Switching Sequence-Based Instantaneous Flux and Current Control for Three-Phase Dual Active Bridge DC–DC Converters

Apoorv Agarwal, *Member, IEEE*, and Subhashish Bhattacharya, *Fellow, IEEE*

***Abstract*—The three-phase dual-active bridge converter is a promising topology for high-power dc–dc conversion applications. Achieving good dynamic performance for DAB3 necessitates control strategies to eliminate dc bias in both transformer current and magnetizing flux linkage during abrupt power changes. However, existing state-of-the-art controls have limitations, such as neglecting the transformer magnetizing flux, current overshoots in wide-voltage gain scenarios, susceptibility to performance degradation with parameter variations, requiring active feedback, or the need for complex and computationally intensive controls. The article addresses these challenges by proposing a switching sequence-based instantaneous flux and current control to ensure no dc bias or overshoot in current and magnetizing flux dynamics for arbitrary load-angle changes in all voltage-gain scenarios. The proposed scheme is independent of the system parameters or operating voltages and is simple to implement. Furthermore, the proposed control can provide seamless integration with established start-up and power-OFF strategies by simultaneously controlling the transformer magnetizing flux and the winding currents. A comprehensive comparison with the conventional instantaneous flux and current control is presented through both simulation and hardware experiment results to validate the proposed control.**

***Index Terms*—Current control, dc bias, flux control, overshoot, switching sequence control, three-phase dual active bridge (DAB3), wide-voltage gain.**

I. INTRODUCTION

THE dual active bridge (DAB) converter has become a popular choice for isolated dc–dc conversion with many desirable characteristics such as galvanic isolation, bidirectional power-flow, soft switching capabilities, and a straight-forward control scheme [1], [2]. As a result, DAB converters have been widely used in various applications. Examples include dc distribution grids [3], [4], as the dc–dc conversion stage within solid state transformers [5], railway electrification [6], electric vehicles (EVs) [7], [8], [9], and grid-interfaced energy storage systems [10], [11], [12], and dc-collector grids for integrating solar and wind farms [13], [14]. For high-power applications, the three-phase DAB (DAB3) offers significant advantages over its single-phase counterpart. The DAB3 configuration, shown in Fig. 1(a), results in lower current stress on individual components and allows for the use of smaller and less expensive filter capacitors compared to single-phase DAB [1].

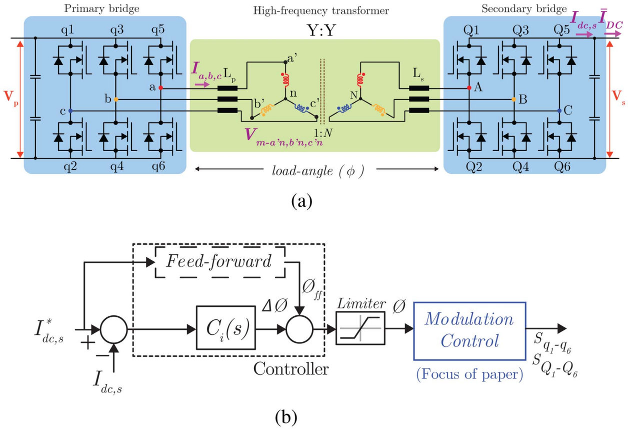

(a)

(b)

Fig. 1. Schematic and control structure of the three phase dual active bridge (DAB3). (a) Schematic. (b) Conventional control structure under the SPS modulation.

The single-phase shift (SPS) modulation strategy is the most common control method employed for DAB3 converters due to its simplicity. The load-angle of the SPS modulation can be dynamically changed to vary the transferred power in the converter. A conventional control structure for regulating power transferred/output current is shown in Fig. 1(b). Based on the current feedback, the load-angle is adjusted through a closed-loop controller, such as a PI or feedforward-based controller. The load-angle is then implemented in the switching signals of the DAB3 converter through a modulation control. However, the conventional modulation control impacts its transient performance, leading to large overshoots and dc bias in the transformer phase currents and magnetizing flux for abrupt load-angle changes [15]. These effects can stress the power semiconductor devices, saturate the magnetic components, and deteriorate the converter's performance.

Different modulation control strategies to implement the load-angle changes have been proposed to achieve dc bias-free control of current and flux linkage for the DAB3 converters. Instantaneous current control (ICC) in [15] and [16] controls the transformer current trajectory using three equal intermediate

---

Received 7 July 2025; revised 23 September 2025; accepted 3 November 2025. Date of publication 7 November 2025; date of current version 19 January 2026. Recommended for publication by Associate Editor S. Tian. *(Corresponding author: Apoorv Agarwal.)*

The authors are with the Department of Electrical and Computer Engineering, North Carolina State University, Raleigh, NC 27606 USA (e-mail: aagarw14@ncsu.edu; sbhatta4@ncsu.edu).

Color versions of one or more figures in this article are available at https://doi.org/10.1109/TPEL.2025.3630809.

Digital Object Identifier 10.1109/TPEL.2025.3630809

angles. It controls the transformer phase currents to reach a new steady state within half a switching cycle without any dc bias. To address the transient dc bias in the transformer magnetizing flux linkage, an instantaneous flux and current control (IFCC) method is presented in [17] and [18]. It supplements the ICC method by introducing a double-sided SPS modulation, where both primary- and secondary-side switching instants are phase-delayed with a distribution factor. This factor is a function of the port voltages and the distribution of inductance across the primary and secondary sides of the transformer to achieve the desired load-angle.

However, for applications where the dc-link voltages can vary over a wide range, such as in the interactions of various energy storage systems [7], [8], [9], [10], [11], [12], or the dc-collector grids for renewable energy [13], [14], the IFCC method suffers from a half-cycle current overshoot albeit no dc bias in abrupt power dynamic conditions [26]. The overshoot can stress the power semiconductor devices and cause magnetic saturation of the series-connected inductor, hindering the reliable operation of the converter. The authors present a model to determine and utilize the overshoot current value to design the components, but it can significantly oversize the converter with up to 50% more current rating required in worst-case scenarios. Furthermore, the load-angle distribution in IFCC requires knowledge of the leakage inductances and feedback of port voltages, resulting in a control that is susceptible to performance degradation with parameter variations. Although IFCC is simple to implement, it is limited by the current overshoots in wide-voltage gain scenarios and sensitivity to system parameters.

Another set of complex controls to address robustness, improve transient performance, and model system complexities have been developed in [22], [23], [24], and [25]. Based on flux control principles for six-step operation in electrical drives, a control method in instantaneous dual flux control (IDFC) [22], generalized instantaneous dual flux control (GIDFC) [23] and instantaneous pulse pattern control (IPCC) [24] have been proposed. While IDFC works for SPS modulation, GIDFC extends it for TPS modulation for duty ranges between 1/6 and 1/3, and IPCC fully encompasses SPS and the entire duty range of TPS. All of these control methods independently regulate the primary and secondary flux linkages with the desired load-angle and duty cycles, achieving dc bias-free flux control. It demonstrates better transient performance, settling within one sampling period, and does not require information on the leakage inductances. However, complex flux control techniques such as dead-beat or model predictive control methods operating with high sampling frequency are required. Also, the implementation of these complex flux control techniques imposes a high computational burden on the controllers. As noted in [24], the combination of high computation demands and the high sampling frequency restricts the method's operable switching frequency to a few kHz (10–15 kHz) on standard DSP-based microcontrollers, such as with a single-core, 200 MHz clock implementation on the TMS28377D microcontroller.

In [25], an artificial neural network (ANN) method-based control is proposed to suppress the dc bias current in the DAB3 converter with variable duty cycle (VDC) modulation. It finds optimal transition angles modeling the nonidealities, such as the winding resistance of the transformer, in simulations, thereby avoiding complex calculations and inaccuracies caused by mathematical approximations, settling within one-third of the switching frequency. However, a key limitation is its failure to address the issues of dc bias in transformer magnetizing flux. Furthermore, it also shows current overshoots for wide-voltage gain scenarios, because it is based on a similar concept, like ICC/IFCC, of implementing intermediate load-angles. A significant drawback of the ANN-based method is the necessity for developing highly accurate simulation models mimicking experimental hardware and then performing extensive simulations to acquire optimal datasets of transient variables to train the ANNs. Consequently, it also increases the control complexity and requires high computational resources, which can be time-consuming and expensive.

The ICC modulation has been further developed for non-SPS modulation-based schemes in [19], [20], and [21]. A fast transient current control (FTCC) for DAB3 converter with VDC modulation strategy is proposed in [19] and [20] and with asymmetrical phase-shift (APS) modulation strategy is proposed in [21]. They are based on similar concepts of applying intermediate duty cycles as proposed in ICC and, thus, also show an overshoot for wide-voltage variation scenarios. Furthermore, it fails to address the dc bias in transformer magnetizing flux, and its efficacy under power reversal conditions is unsubstantiated.

Different from the above methods, a few switching sequence-based control methods [17], [27] for the DAB3 converter have been proposed for start-up and power-OFF operations. The dc-bias flux linkage can also be induced in these other transient situations. A straight-path technique at zero load-angle is shown in [17] by modifying the switching state sequence to ensure no dc bias is induced. Von den Hoff and De Doncker [27] extended it to get fully soft-switched start-up/power-OFF operations at nonzero load-angles. However, these methods require a combination of separate modulation techniques for steady-state operation and start-up/power-OFF operations, making it a challenging aspect.

Table I tabulates a comparative summary of the existing and the proposed current control strategies for the DAB3 converter. The existing control strategies exhibit different shortcomings—ranging from neglecting the transformer magnetizing flux to current overshoots in wide-voltage gain scenarios, sensitivity to parameter variations, requiring high control complexity, or reliance on separate modulation strategies for start-up/power-OFF operation. The article proposes a switching sequence-based instantaneous flux and current control (SS-IFCC) for SPS modulated DAB3 converter to address all the above challenges collectively. The proposed SS-IFCC has the following advantages:

1) *Universal control:* It ensures no dc bias or overshoot in both current and magnetizing flux dynamics for arbitrary load-angle change and even power reversal scenarios across the entire voltage-gain operating range.
2) *A robust control:* It is independent of the information of system parameters or operating voltages to ensure zero dc bias magnetizing flux. This independence eliminates the reliance on precise measurements of inductor values, which can vary due to manufacturing tolerances,

TABLE I
OVERVIEW OF THE EXISTING AND PROPOSED CURRENT CONTROL STRATEGIES FOR THE THREE-PHASE DAB CONVERTER

Reference	**Year**	**Controls magnetizing flux**	**Wide-voltage gain scenarios**	**Robust to system parameters**	**Control complexity**	**Start-up/Power-off strategy**
ICC [15], [16]	2013-14	×	×	×	Low	×
IFCC [17], [18]	2020-21	✓	×	×	Low	✓†
FTCC [19]–[21]	2017-23	×	×	×	Low	×
IDFC [22], GIDFC [23], IPCC [24]	2023-25	✓	Not shown	✓	High	Not shown
ANN-based control [25]	2025	×	Not shown	✓	High	×
Proposed SS-IFCC	–	✓	✓	✓	Low	✓

† (requires separate modulation strategy)

temperature fluctuations, and aging. It also avoids the need for continuous feedback of input or output port voltages.

3) *Straightforward control*: It is simple to implement and does not require high computation capabilities or employ complex control techniques. It eliminates the need for complex real-time calculations or intermediate/transition load-angle estimations.

4) The start-up/power-OFF procedure for the DAB3 converter proposed in [17] can be seamlessly integrated into the proposed scheme.

A comprehensive comparison of the conventional IFCC method with the proposed SS-IFCC method is provided. The conventional IFCC method offers a simple implementation for current and flux control for the DAB3 converter and does not require high sampling frequencies, complex techniques, or extensive training data. Extensive simulation and hardware experiment results on a DAB3 converter for a battery system with a wide voltage variation (270–400 V), operating at 50-kHz switching frequency, are provided to validate and highlight the advantages of the proposed SS-IFCC.

In Section II, the modeling of the current and flux trajectory for the DAB3 is briefly revisited for better understanding. Following this, the performance of the conventional IFCC under wide voltage variation and its dependence on system parameters knowledge is analyzed in Section III. The proposed SS-IFCC method is described in Section IV, followed by the simulation and experimental validation in Section V. Finally, the conclusion is given in Section VI.

II. MODELING OF TRANSFORMER CURRENT AND FLUX IN DAB3

DAB3 converter is shown in Fig. 1(a), with primary and secondary port dc-link voltages, V_p and V_s, respectively. It comprises two three-phase bridges linked by a star-connected three-phase high-frequency transformer (HFT) having a turns ratio N, and a series-inductors arrangement L_p and L_s. The gain of the converter d is represented by

$$d = V_s/(NV_p). \tag{1}$$

In the DAB3 SPS modulation strategy, both three-phase bridges operate with a fixed 0.5-duty cycle. Each three-phase bridge has six switching states ⓡ in a switching period, shown in Table II. Each phase (q_1, q_2, q_3) is 1 or 0 to represent when the upper or lower switch is conducting, respectively. These switching states ⓡ produce the three-phase voltages at transformer terminals. When transformed into $\alpha\beta$ coordinates, a space vector $\vec{k_r}$ can represent each switching state, as shown in Fig. 2(a). Thus, the transformed three-phase voltages in $\alpha\beta$ coordinates is $\vec{u_r} = V.\vec{k_r}$ for each switching state r, where V is the dc-link voltage.

TABLE II
SWITCHING STATE OF A BRIDGE IN DAB3

r	①	②	③	④	⑤	⑥
q_1	1	1	0	0	0	1
q_2	0	1	1	1	0	0
q_3	0	0	0	1	1	1
$\vec{k_r}$	$\frac{2}{3}e^{j0^\circ}$	$\frac{2}{3}e^{j60^\circ}$	$\frac{2}{3}e^{j120^\circ}$	$\frac{2}{3}e^{j180^\circ}$	$\frac{2}{3}e^{j240^\circ}$	$\frac{2}{3}e^{j300^\circ}$

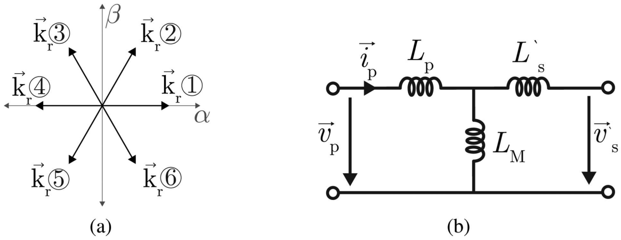

Fig. 2. Simplified equivalent circuit of the DAB3 converter in $\alpha\beta$ coordinates. (a) Unity voltage vector of a three-phase bridge. (b) Simplified equivalent circuit of the three-phase transformer.

The three-phase transformer in the DAB3 converter can also be modeled by an equivalent circuit in $\alpha\beta$ coordinates, as shown in Fig. 2(b). L_p, L'_s, and L_M denote the primary-side series, secondary-side series, and magnetizing inductance, all referred to the primary side. The primary and secondary bridge voltage vectors, $\vec{v_p} = V_p.\vec{k_r}$ and $\vec{v_s} = V_s.\vec{k_r}$, are applied across the circuit, phase-shifted with a load-angle ϕ. It results in the phase current $\vec{i_p}$ flowing through the primary-side inductance and the voltage $\vec{u}_M$ across the magnetizing inductance, thus controlling the transferred power. The steady-state switching waveform of the DAB3 converter with SPS modulation strategy is shown in Fig. 3. The steady-state switching sequence is q = ⑥→ ①→ ②→ ③→ ④→ ⑤, referenced to the primary-side bridge operation.

The transformer current and magnetizing flux trajectories in $\alpha\beta$ coordinates have been modeled in [15], [16], [17], [18], [26].

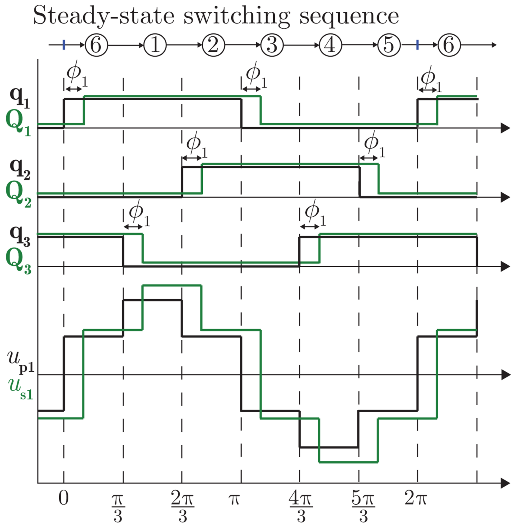

Fig. 3. Steady-state switching waveforms of DAB3.

The work is briefly reproduced to provide a foundation for the proposed control. Using the equivalent circuit in Fig. 2(b), the slope of the primary-side current change and magnetizing flux-linkage change for given switching states m for the primary bridge and n for the secondary bridge is

$$\frac{d\vec{i}_{p,m/n}}{dt} = \frac{\vec{u}_{p,m}}{L_1} - \frac{\vec{u}_{s',n}}{L_2} \tag{2}$$

$$\frac{d\vec{\psi}_{M,m/n}}{dt} = \vec{u}_{M,m/n} = \lambda_1 \cdot \vec{u}_{p,m} + \lambda_2 \cdot \vec{u}_{s',n} \tag{3}$$

where, for $L_M \gg L_p, L'_s$, the terms are

$$L_1 = L_2 = L_p + L'_s = L; \text{ and } \lambda_1 = \frac{L'_s}{L}; \lambda_2 = \frac{L_p}{L}. \tag{4}$$

In the DAB3 SPS operation, for a switching state n of the primary bridge, the secondary bridge is switched from state m to n, delayed with a load-angle ϕ. Therefore, the variation of the primary current and flux linkage between two successive switching states of the primary bridge is

$$\Delta\vec{i}_{p,m\to n}(\phi) = \frac{\phi}{2\pi f} \cdot \frac{d\vec{i}_{p,n/m}}{dt} + \frac{\pi/3 - \phi}{2\pi f} \cdot \frac{d\vec{i}_{p,n/n}}{dt} \tag{5}$$

$$= \phi \cdot \vec{A}_{i,n/m} + (\pi/3 - \phi) \cdot \vec{B}_{i,n/n} \tag{6}$$

$$\Delta\vec{\psi}_{M,m\to n}(\phi) = \frac{\phi}{2\pi f}\frac{d\vec{\psi}_{M,n/m}}{dt} + \frac{\pi/3 - \phi}{2\pi f}\frac{d\vec{\psi}_{M,n/n}}{dt} \tag{7}$$

$$= \phi \cdot A_{\psi,n/m} + (\pi/3 - \phi) \cdot B_{\psi,n/n} \tag{8}$$

$$\text{where, } \vec{A}_{i,n/m} = c \cdot \left[\vec{k}_n - d \cdot \vec{k}_m\right]; \tag{9}$$

$$\vec{B}_{i,n/n} = c \cdot (1-d) \cdot \left[\vec{k}_n\right]; \; c = 2V_p/(6\pi f L); \tag{10}$$

$$A_{\psi,n/m} = \frac{V_p}{2\pi f L}\left(L_{s'} \cdot \vec{k}_n + L_p \cdot d \cdot \vec{k}_m\right) \tag{11}$$

$$B_{\psi,n/n} = \frac{V_p}{2\pi f L}(L_{s'} + L_p \cdot d)\vec{k}_n. \tag{12}$$

Moreover, as $\vec{k}_{r+1} = \vec{k}_r . e^{j60^\circ}$, it can be shown that

$$\Delta\vec{i}_{p,n\to(n+1)}(\phi) = \Delta\vec{i}_{p,(n-1)\to n} . e^{j60^\circ}(\phi) \tag{13}$$

$$\Delta\vec{\psi}_{M,n\to(n+1)}(\phi) = \Delta\vec{\psi}_{M,(n-1)\to n} . e^{j60^\circ}(\phi). \tag{14}$$

Thus, the steady-state trajectory of both the primary current and magnetizing flux linkage form a regular hexagon shape centered around the origin in $\alpha\beta$ coordinates with the length of each edge determined by the load-angle ϕ. The trajectories of transformer currents and magnetizing flux linkage for different d's are shown in Fig. 4. The modeling shows the symmetric trajectories of the current and flux linkage for the switching states, which will be utilized to develop the proposed method.

III. PERFORMANCE OF CONVENTIONAL IFCC

The conventional IFCC method proposed in [17] controls the transient trajectory of the transformer current and the magnetizing flux to reach the new steady state without any dc bias. For a load-angle change from ϕ_1 to ϕ_2, three equal intermediate load-angle of $\phi_{t1} = \phi_{t2} = \phi_{t3} = \frac{\phi_1+\phi_2}{2}$ are implemented, as shown in Fig. 5. It controls the transformer current dynamics from the initial to the target trajectory without any dc bias. This concept can be verified by calculating the transformer current in the transient state using (6) and (13) as

$$\overbrace{\overbrace{\vec{i}_{p,5}(\phi_1) + \Delta\vec{i}_{p,5\to 6}\left(\frac{\phi_1+\phi_2}{2}\right)}^{\vec{i}_{p,t1}} + \Delta\vec{i}_{p,6\to 1}\left(\frac{\phi_1+\phi_2}{2}\right)}^{\vec{i}_{p,t2}}$$

$$+ \Delta\vec{i}_{p,1\to 2}\left(\frac{\phi_1+\phi_2}{2}\right) = \vec{i}_{p,t3} = \vec{i}_{p,2}(\phi_2). \tag{15}$$

Further, to control the flux dynamics without any dc bias, it implements a double-sided SPS modulation scheme, in which the primary- and secondary-side switching instants are varied with a distribution factor *p*

$$p = \frac{L_p V'_s}{L_p V'_s + L'_s V_p}. \tag{16}$$

Using the double-sided SPS modulation with *p*-factor, the dc-bias flux linkage component induced by the primary side cancels out the component induced by the secondary side. Thus, provided the port voltage and series-inductance values are accurately known, the conventional IFCC ensures zero dc-bias flux linkage for each switching step. However, the series-inductance value measurement can have errors due to manufacturing tolerances, temperature fluctuations, and aging. Consequently, the p-factor will deviate from its correct value, resulting in flux overshoots and potentially saturating the transformer.

Further, the three equal intermediate load-angles proposed in the conventional IFCC method can only guarantee zero dc bias in the transformer current for the step load-angle change and do not account for transient currents. The authors in [26] have shown that the conventional IFCC modulation can have a current overshoot under wide-voltage gain scenarios ($d \neq 1$). The overshoot can stress the power semiconductor devices and

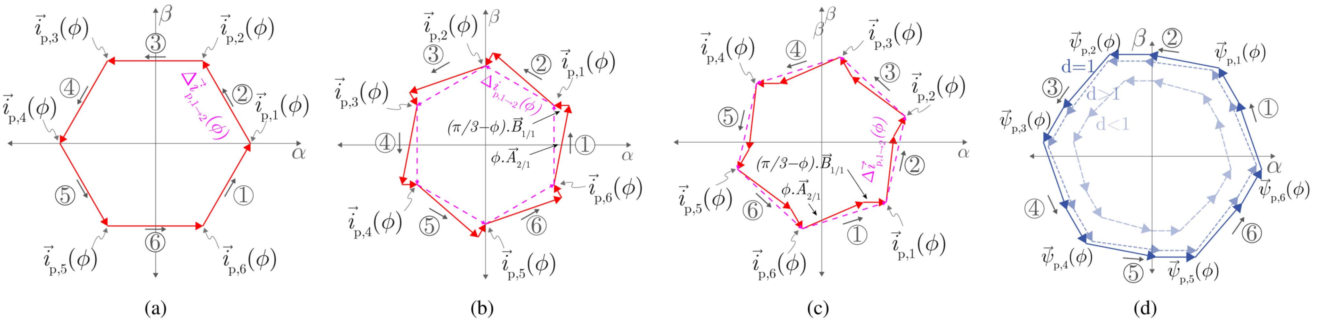

Fig. 4. Trajectories of steady-state transformer currents and flux in $\alpha\beta$ coordinates for different gains. (a) Current $d = 1$. (b) Current $d > 1$. (c) Current $d < 1$. (d) Transformer flux.

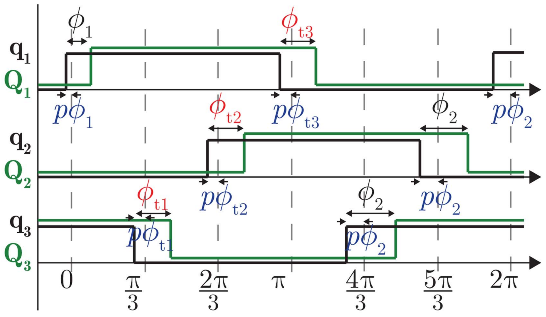

Fig. 5. Switching signals for double-sided SPS modulation based conventional IFCC [17].

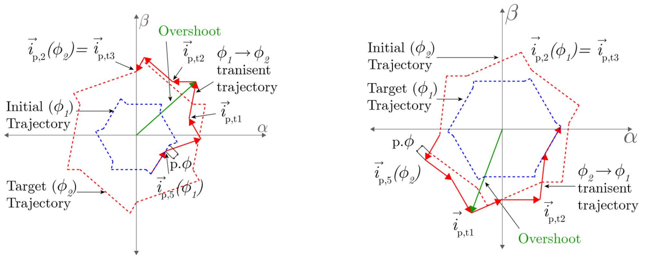

Fig. 6. Trajectories of transformer currents with a load-angle change ($\phi_2 > \phi_1$) in $\alpha\beta$ coordinates for d $\neq$1 with conventional IFCC [26]. (a) Conventional IFCC: d $>$ 1. (b) Conventional IFCC: d $<$ 1.

cause magnetic saturation of the series-connected inductor. The transformer phase currents and flux still reach the new steady state within half a switching cycle without any induced dc bias.

Fig. 6 shows the transformer current in the $\alpha\beta$ coordinate system with the conventional IFCC method for a load-angle change ($\phi_2 > \phi_1$) with $d > 1$ and $d < 1$. The transformer current trajectory reaches the new steady state within about half a switching cycle, showing fast settling of the transformer currents irrespective of the value of d. No dc bias is induced in the currents in any case. However, the transient current trajectory can have an overshoot, denoted by the green vector. In [26], a model is presented to determine the overshoot current value for known system parameters and load-angle step-change scenarios. It is proposed that the value be utilized to select the core saturation peak current rating of the series-connected inductors and the peak current through the devices for a robust design and operation of the converter.

However, the conventional IFCC can cause a worst-case overshoot of up to 50% more than the rated current operation for scenarios such as when power reversal is needed for a DAB3 converter operating with nonunity voltage gain and inductance distributed on one side. It requires significantly oversized series-connected inductors and devices for a robust converter operation. Thus, this article proposes a new modulation scheme to ensure no dc bias or overshoot in current and magnetizing flux dynamics for arbitrary load-angle change in all unity and nonunity voltage-gain scenarios.

IV. PROPOSED SWITCHING SEQUENCE-BASED INSTANTANEOUS FLUX AND CURRENT CONTROL

The IFCC modulation ensures the current/flux trajectories in $\alpha\beta$ coordinates from the initial trajectory reach the target trajectory without any dc bias. However, the problem in the control is the unknown positions of the current and flux trajectories during the intermediate load-angles. Thus, a current overshoot is observed with IFCC modulation in nonunity gain scenarios.

The proposed SS-IFCC scheme addresses the problem. It is based on modifying the initial two switching states of the steady-state switching sequence of the converter when a load-angle change is initiated. As previously mentioned, the steady-state switching sequence of a DAB3 converter is q = ⑥→ ①→ ②→ ③→ ④→ ⑤, referenced to the primary-side bridge operation. In the proposed SS-IFCC, upon a required load-angle change from $\phi_1 \rightarrow \phi_2$, the switching states ① and ⑥ are interchanged from the steady-state switching sequence and operated with ϕ_1 and ϕ_2, respectively. In the proposed scheme, this switching sequence change is initiated at the start of the switching sequence, i.e., after the switching state ⑤ of the previous switching period.

During the first transient switching state ①, the current/flux trajectories in $\alpha\beta$ coordinates are driven to the origin (0) from the initial trajectory. Subsequently, in the transient next switching state ⑥, these current/flux trajectories in $\alpha\beta$ coordinates are driven to the target trajectory, ensuring that no dc bias is induced. Thus, the current/flux coordinates are always encapsulated by the maximum of the trajectories, preventing any overshoot.

Fig. 7 shows the switching waveforms for the proposed SS-IFCC method. The corresponding transformer current and flux

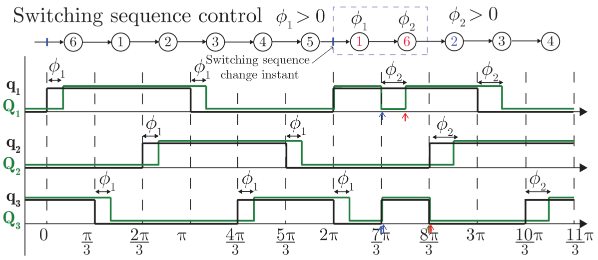

Fig. 7. Switching signals for SS-IFCC modulation ($\phi_1, \phi_2 > 0$).

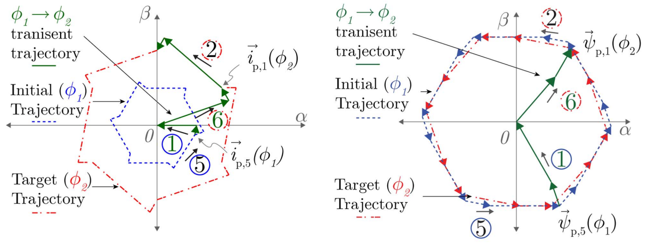

(a) (b)

Fig. 8. Trajectories of transformer currents and magnetizing flux with a load-angle change ($\phi_1, \phi_2 > 0$) in $\alpha\beta$ coordinates with proposed SS-IFCC. (a) SS-IFCC: Transformer current. (b) SS-IFCC: Transformer flux.

trajectory in the $\alpha\beta$ coordinates is shown in Fig. 8. Utilizing the symmetric nature of the current/flux trajectories, the switching state ① operated with initial load-angle (ϕ_1), drives the trajectories ($\Delta\vec{i}_{p,6\rightarrow 1}(\phi_1)$) to origin from the end position of the switching state ⑤. Then, the switching state ⑥ operated with target load-angle (ϕ_2), drives the trajectories ($\Delta\vec{i}_{p,5\rightarrow 6}(\phi_2)$) to the target trajectory from the origin. After, it continues with the remaining steady-state switching sequence of ② → ③ → ④ → ⑤ with the target load-angle and repeats with the normal steady-state switching sequence. The proposed SS-IFCC is applied only when a load-angle change is required; the steady-state switching sequence and thus, steady-state operation, remain unaffected.

In the proposed SS-IFCC, current or flux positions are always known and bound; thus, no overshoot exists, irrespective of the change in load-angle and the gain (d) of the converter. The zero dc bias feature can be verified by calculating the transformer current and flux positions using (6) and (13) as

$$\overbrace{\vec{i}_{p,5}(\phi_1) + \Delta\vec{i}_{p,6\rightarrow 1}(\phi_1)}^{0} + \Delta\vec{i}_{p,5\rightarrow 6}(\phi_2) = \vec{i}_{p,1}(\phi_2) \tag{17}$$

$$\overbrace{\vec{\psi}_{M,5}(\phi_1) + \Delta\vec{\psi}_{M,6\rightarrow 1}(\phi_1)}^{0} + \Delta\vec{\psi}_{M,5\rightarrow 6}(\phi_2) = \vec{\psi}_{M,1}(\phi_2). \tag{18}$$

Also, the proposed SS-IFCC method is simple to implement. The switching actions required are already known, corresponding to the switching state and load-angle as shown in Table II and consequently, straightforward to implement in the controller. Furthermore, the proposed method is effective independent of load-angle, system parameters, and input and output port voltages. Using the symmetric nature of the current and flux trajectories, both are simultaneously controlled without the need for any additional factor. Thus, the proposed SS-IFCC method provides a robust control compared to the conventional IFCC method, which is sensitive to inaccuracies in port voltage measurements or manufacturing tolerances of the series-connected inductor values.

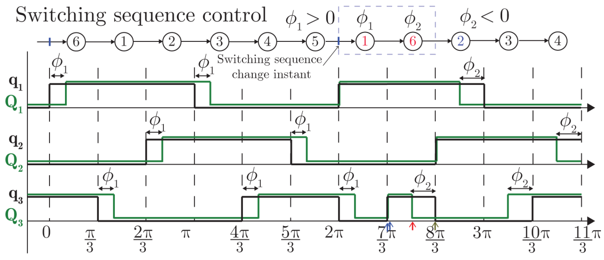

Fig. 9. Example of proposed SS-IFCC modulation for power reversal scenarios ($\phi_1 > 0, \phi_2 < 0$).

The SS-IFCC method also functions for the power reversal scenarios with zero dc bias and overshoot in currents and flux for any arbitrary gain of the converter. The switching waveforms of SS-IFCC for the power reversal scenario are shown in Fig. 9 with $\phi_1 > 0, \phi_2 < 0$. With the proposed SS-IFCC, switching state ① operates with the positive load-angle ($\phi_1 > 0$) and the switching state ⑥ operates with the negative load-angle ($\phi_2 < 0$), seen in the q3 and Q3 waveforms between 2π and $8\pi/3$.

In [17], two different techniques are combined, one in a soft magnetization/demagnetization technique for the start-up and power-OFF operation, and another technique in a double-sided SPS-based IFCC method for the load-angle changes during operation. However, the start-up and power-OFF operations in [17] can be seamlessly integrated with the proposed SS-IFCC, with both based on modifying the switching sequences.

For start-up with SS-IFCC, state ① is skipped, initiating the switching sequence from state ⑥ and continues with the remaining steady-state switching sequence of ② → ③ → ④ → ⑤ and repeating with normal steady-state switching sequence. The SS-IFCC start-up switching signals with the load-angle ϕ of 0 are shown in Fig. 10(a). As previously noted, state ⑥ drives the current/flux trajectories from the origin to the steady state, as shown in Fig. 11. Similarly, for power-OFF operation, the SS-IFCC utilizes only the first switching state ① in the sequence, which drives the current/flux trajectories to the origin before all the switches are turned OFF. The SS-IFCC power-OFF switching signals are shown in Fig. 10(b), assuming a load-angle ϕ of 0 before the converter is powered-OFF.

The proposed SS-IFCC does have a tradeoff with all its advantages. It imposes additional switching instances compared to the conventional IFCC method, indicated by the arrows in Fig. 7. It shows six additional switching instances—two on the primary and four on the secondary bridge, when the load-angle is changed from $\phi_1 > 0$ to $\phi_2 > 0$. It can be observed that three of the instances, $q_1 \downarrow$, $q_3 \uparrow$, $Q_3 \uparrow$ (indicated by blue arrows), occur at zero-current, showing zero current switching (ZCS) and one other instance, $q_3 \downarrow$ (indicated by brown arrows), shows zero voltage switching (ZVS) with the topology operation as analyzed using [1], [27]. Thus, only two instances, $Q_1 \uparrow$, $Q_3 \downarrow$ (indicated by red arrows), are hard-switched. A similar analysis for

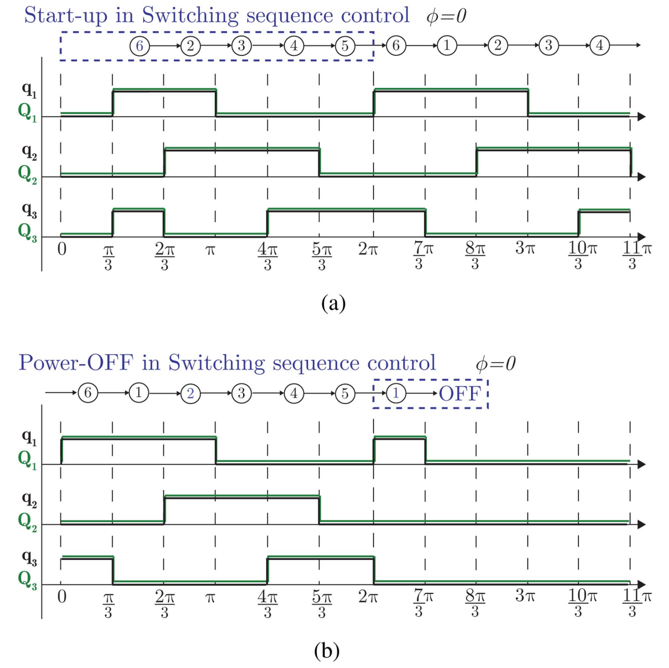

Fig. 10. Switching signals for start-up and power-OFF with the proposed SS-IFCC. (a) Start-up. (b) Power-OFF.

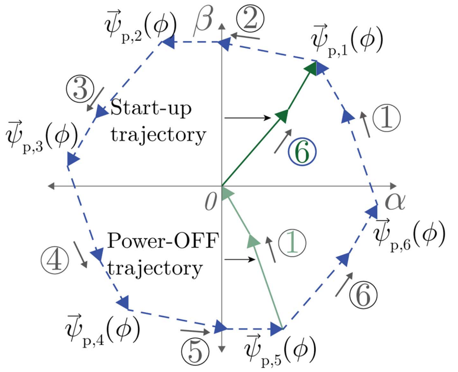

Fig. 11. Trajectories of transformer magnetizing flux in $\alpha\beta$ coordinates for start-up and power-OFF with the proposed SS-IFCC.

other load-angle change scenarios, such as power reversal (see Fig. 9), also shows only one additional hard-switched instance, with the rest being soft-switched. Furthermore, these additional one/two hard-switched instances and other soft-switched instances in the proposed SS-IFCC method are applied in the transient state only, when a load-angle change is required; the steady-state switching sequence and thus, steady-state operation, remains unaffected. Consequently, there is no loss in steady-state operation efficiency with the proposed SS-IFCC method.

However, even with a constant reference signal, minor noise from sources like switching ripple, component imperfections, and sensors can cause the feedback signal to fluctuate. This fluctuation leads to a small, nonzero error signal, which in turn causes the controller's output (load-angle) to oscillate minimally around its ideal value. Without a mitigation strategy, these small oscillations would incessantly trigger the proposed scheme, leading to unnecessary switching actions and continuously altering the current and flux trajectory, thereby compromising efficiency and stability. This issue is not unique to the proposed method; other dc-bias-free control strategies for DAB3 converters face similar challenges from steady-state load-angle oscillations.

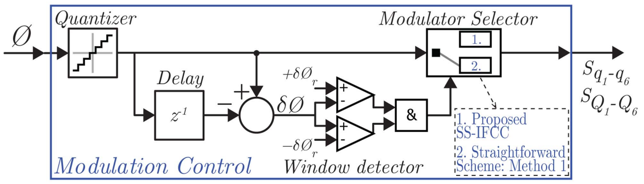

Fig. 12. Control structure of the unified modulation control.

To address this issue, a unified modulation control scheme is implemented, as shown in Fig. 12. It implements a quantizer, which reflects that in a digital implementation, the load-angle can only change in discrete steps. If the noise-induced oscillations are smaller than this minimum step size, the load-angle remains constant, effectively ignoring the noise. Further, it integrates the proposed SS-IFCC method for the transient operation with a simple, feedback-free, traditional scheme for the steady-state operation. The scheme differentiates between transient and steady-state operations, based on a minimum threshold for the load-angle change, denoted as $|\delta\phi_r|$, using a window detector. If the change in load-angle is larger than $|\delta\phi_r|$, the proposed SS-IFCC method is activated to ensure fast, precise transient response. Conversely, if the change is smaller than the threshold, the system is considered to be in a steady state, and a straightforward scheme is employed. The straightforward scheme can be chosen as Method 1 in [15], which changes the load-angle of all phases at the same edge. Although it can cause large flux and current overshoots for large load-angle changes, it is well-suited to provide dc-bias suppression for small adjustments in load-angle ($< |\delta\phi_r|$), and effectively avoids the incessant switching caused by noise.

The threshold value of $|\delta\phi_r|$ is carefully selected based on the system's sensitivity, ensuring that load-angle changes in steady-state operation do not significantly impact power flow. This unified approach ensures seamless performance across both transient and steady-state operations, with the proposed SS-IFCC offering its advantage for larger load-angle changes, providing a straightforward implementation, universal applicability across all voltage gain scenarios, and inherent robustness as it functions independently of converter parameters.

V. SIMULATION RESULTS AND HARDWARE DEMONSTRATION

A. Simulation Results

The DAB3 converter is simulated using the PLECS circuit simulation software with the parameters listed in Table III to validate the analysis and compare the performance of the proposed SS-IFCC method with the conventional IFCC method. A DAB3 converter for a battery system with a wide voltage variation (270–400 V) is considered. Three scenarios with two nonunity

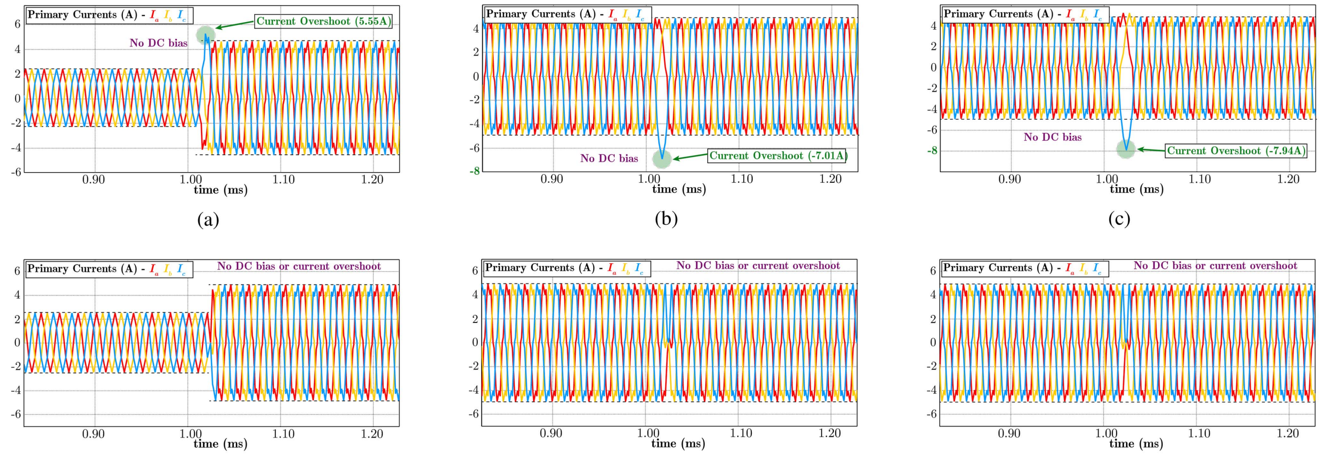

(a) (b) (c)

(d) (e) (f)

Fig. 13. Simulation Results: Transformer primary currents for different case scenarios. (a) Conventional IFCC control, Case I. (b) Conventional IFCC control, Case II. (c) Conventional IFCC control, Case III. (d) SS-IFCC control, Case I. (e) SS-IFCC control, Case II. (f) SS-IFCC control, Case III.

TABLE III
DAB3 SPECIFICATIONS

Parameter	Value
Rated Power, P	2 (kW) at $\phi = 40°$
Primary DC-link Voltage, V_p	270–400 (V)
Secondary DC-link Voltage, V_s	270–400 (V)
Switching frequency, f_s	50 (kHz)
Turns Ratio, N	1
Magnetizing inductance, L_m	3 (mH)
Transformer leakage inductance, L_{lk}	11 (μH)
Primary-side series inductance, L_p	50 (μH)
Secondary -side series inductance, L_s	50 (μH)

voltage gain and different inductance distributions are simulated. An equal distribution of the inductances on the primary and secondary sides ($L_p = L_s = 50\ \mu$H) is considered for the first two cases—Case I: $V_p = 270$ V, $V_s = 400$ V ($d = 1.48$), with a load-angle change from $0° \to 40°$ and Case II: and $V_p = 400$ V, $V_s = 270$ V ($d = 0.675$) with $40° \to -40°$. Case III considers the scenario where all the inductance is distributed to the primary side for $d = 0.675$ and load-angle change of $40° \to -40°$ to demonstrate the worst-case current overshoot. In all cases, an inherent leakage inductance of 11 μH resulting from the HFT is considered, to match the parameters used in the hardware.

The simulation results for the conventional IFCC method are shown in Fig. 13(a)–(c). Due to different port voltages and the inductance distribution, different distribution p-factors are implemented for each scenario: $p = 0.4$ for Case I, $p = 0.6$ for Case II, and $p = 1$ for Case III. Results show that a large overshoot current with no dc bias is induced in the primary current during the load-angle changes with the conventional IFCC method in a nonunity voltage gain scenario. Compared to the 5.37 A peak current operation for the rated power, a current overshoot of 5.55 and 7.01 A is noted for the first two scenarios, resulting in a $\approx$3% and $\approx$ 30% higher rating, respectively. In case III, where all inductance is distributed to the primary side, a current overshoot of 7.92 A is observed, resulting in a $\approx$50% higher rating required compared to the same baseline. Significantly oversizing the series-connected inductors and devices with up to 50% higher peak current rating would be required to account for these scenarios with the conventional IFCC method.

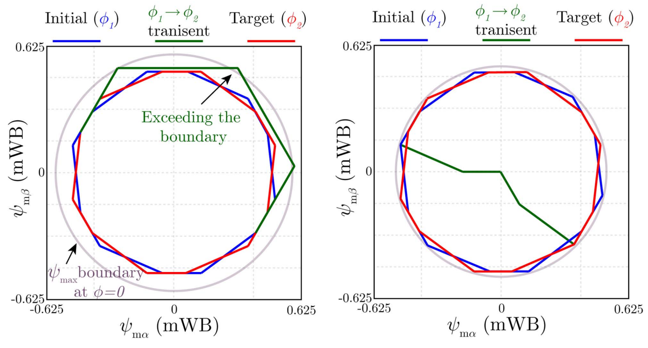

(a) (b)

Fig. 14. Simulation results: Trajectories of transformer magnetizing flux ($\alpha\beta$ coordinates), for Case II, with inductor measurement error (-5%:primary side, $+5$%:secondary side). (a) Conventional IFCC control. (b) SS-IFCC control.

Fig. 13(d)–(f) shows the simulation results with the proposed SS-IFCC method present excellent control performance. Compared with the IFCC method, no current overshoot occurs with the proposed method. The three-phase currents are simultaneously driven to the origin(zero) in the first switching state, then to the target steady state, avoiding any dc bias or overshoot.

Another scenario was simulated for Case II to examine the impact of inductance measurement errors, introducing a -5% and $+5$% error in the primary-side and secondary-side inductor measured values, respectively. The transformer magnetizing flux in $\alpha\beta$ coordinates is shown in Fig. 14 for both the conventional IFCC and the proposed SS-IFCC methods. Fig. 14(a) shows that the conventional IFCC method exhibits a transient overshoot in the transformer magnetizing flux for the load-angle change when an error (-5%: primary side, $+5$%: secondary side) in the inductor's measured value is present. The overshoot is due to

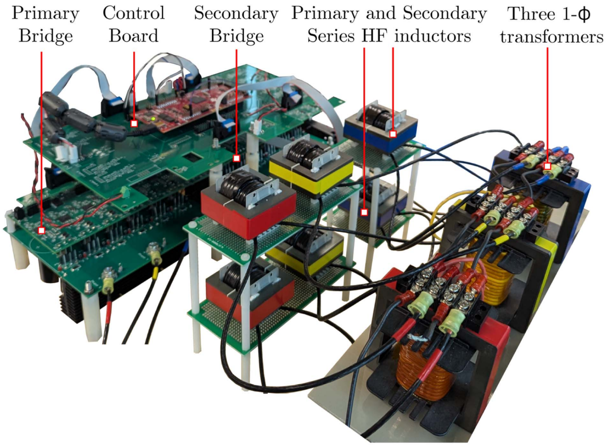

Fig. 15. Experimental setup.

the inaccuracies in the determined distribution p-factor, which is based on precise inductance measurements. If the flux linkage overshoot exceeds the limit value of the saturation flux linkage, the transformer core will saturate. In contrast, the proposed SS-IFCC method shown in Fig. 14(b) effectively controls the magnetizing flux within the bounds. The robustness to inductor measurement error of the proposed method is by virtue of its independence from port voltage feedback and inductance distribution information, demonstrating the superior resilience of the proposed SS-IFCC method.

B. Hardware Demonstration

The proposed SS-IFCC modulation strategy is implemented and validated on a ≈2-kW rated hardware setup of the DAB3 converter, as shown in Fig. 15, with the same specifications as for the simulations, as listed in Table III. The two three-phase bridges employ 650 V SiC devices. Two bidirectional dc power supplies: Chroma 62180D-1200 and ITECH IT6018C-1500-40 are utilized for the input/output port voltages. The proposed SS-IFCC control and conventional IFCC are implemented on a TI F28379D DSP-based microcontroller (single-core) with a 200-MHz system clock frequency. In the DSP implementation, the EPWM module with its four compare registers is implemented to set the PWM signals. With switching action within a switching state fixed (ⓝ- Table II), interrupts are generated at strategic points to drive the modifications of the PWM signals, without affecting the control execution time or any glitches. A star–star configuration is used for three single-phase HFTs, and external series-inductors are utilized to achieve the series inductances on both the primary and secondary sides. The turns ratio N of the HFT is chosen as 1, according to the dc-link voltages on either side of the converter, to ensure ZVS for the maximum power range. The gain of the converter varies according to the dc-link voltages of the ports. Both HFTs and series-inductors are built using ferrite material 3C95 with E-shaped cores E80/38/20 and E65/32/27, respectively. The maximum flux density (Bmax) of the core is designed to be 0.2 T. The primary and secondary winding of the HFT is made up of 19 turns, and the inductor winding is made of 9 turns with cores having an air gap. The inductors and the device's current rating are sized to allow for the current overshoots in the conventional IFCC method.

Similar to simulations, two scenarios with different nonunity voltage gains are considered: i) $d = 1.48$: $V_p = 270$ V, $V_s = 400$ V, with a load-angle change of $\phi = 0^\circ \rightarrow 40^\circ$, showing power step-up and ii) $d = 0.675$: $V_p = 400$ V, $V_s = 270$ V, with a load-angle change of $\phi = 40^\circ \rightarrow -40^\circ$, showing power reversal. Fig. 16 shows the experimental results with the conventional IFCC and the proposed SS-IFCC method for the two scenarios. The instantaneous output port current flowing into the capacitor I_{dc-s}, a representative average output dc current flowing to the output port $\bar{I}_{DC}$, along with the transformer primary currents $I_{a,b,c}$, and the transformer magnetizing voltages at the primary windings of the transformer $V_{m-a'n,b'n,c'n}$, as indicated in Fig. 1(a), are measured and plotted in the time domain. In addition, the three-phase transformer currents and transformer magnetizing flux linkage are represented in the $\alpha\beta$ coordinates for the different scenarios. The flux linkage is derived by integrating the measured voltages $V_{m-a'n,b'n,c'n}$, divided by the number of turns. Blue and red colored waveforms present the steady-state trajectories, whereas green waveforms represent the transient trajectory with the method implemented—conventional IFCC or the proposed SS-IFCC method.

Fig. 16(a), (c), and (d) shows the experimental results with the conventional IFCC method for $d = 1.48$, $\phi = 0^\circ \rightarrow 40^\circ$. Based on inductor distribution and port voltages, a p-factor of 0.4 is employed. The average output dc current $\bar{I}_{DC}$ steps up at the triggered instant shown by the dotted vertical line, reflecting the step-up in the power, with the voltage being held constant by the bidirectional power supply. The ripple in the instantaneous output port current $I_{\mathrm{dc}-s}$ increases with the load-angle. Although the conventional IFCC method achieves the transient control of the transformer currents reaching the new steady-state with no dc bias, a current overshoot of 5.52 A [see Fig. 16(a)] is observed, exceeding the peak current operation of 5.37 A at rated power (an increase of ≈3%). With the conventional IFCC, the trajectories of transformer currents and magnetizing flux [see Fig. 16(c) and (d)] reach the new steady-state by applying three intermediate load-angles during the transient. It is realized without any dc-bias in transformer currents or magnetizing flux-linkages, but shows a current overshoot.

Fig. 16(g), (i), (j) shows the same conditions of $d = 1.48$, $\phi = 0^\circ \rightarrow 40^\circ$ with the proposed SS-IFCC method. The ripple of the instantaneous output port current I_{dc-s} changes according to the switching state and the rectified HFT currents. Even though the instantaneous output port current I_{dc-s} exhibits an irregular pattern, the capacitor at the output port filters the ripple, with the average output dc current $\bar{I}_{DC}$ supplied to the output port. Notably, no current overshoot or dc bias is observed in the transformer currents. With the proposed method, the transient current and flux trajectories in $\alpha\beta$ coordinates [Fig. 16(i), (j)] move to the origin from the initial trajectory and then to the target trajectory without any dc bias or overshoot and are always enclosed in the maximum value envelope.

For the other scenario of $d = 0.675$, $\phi = 40^\circ \rightarrow -40^\circ$, Fig. 16(b), (e), (f) show the results with the conventional IFCC method. A p-factor of 0.6 is employed for the scenario. The

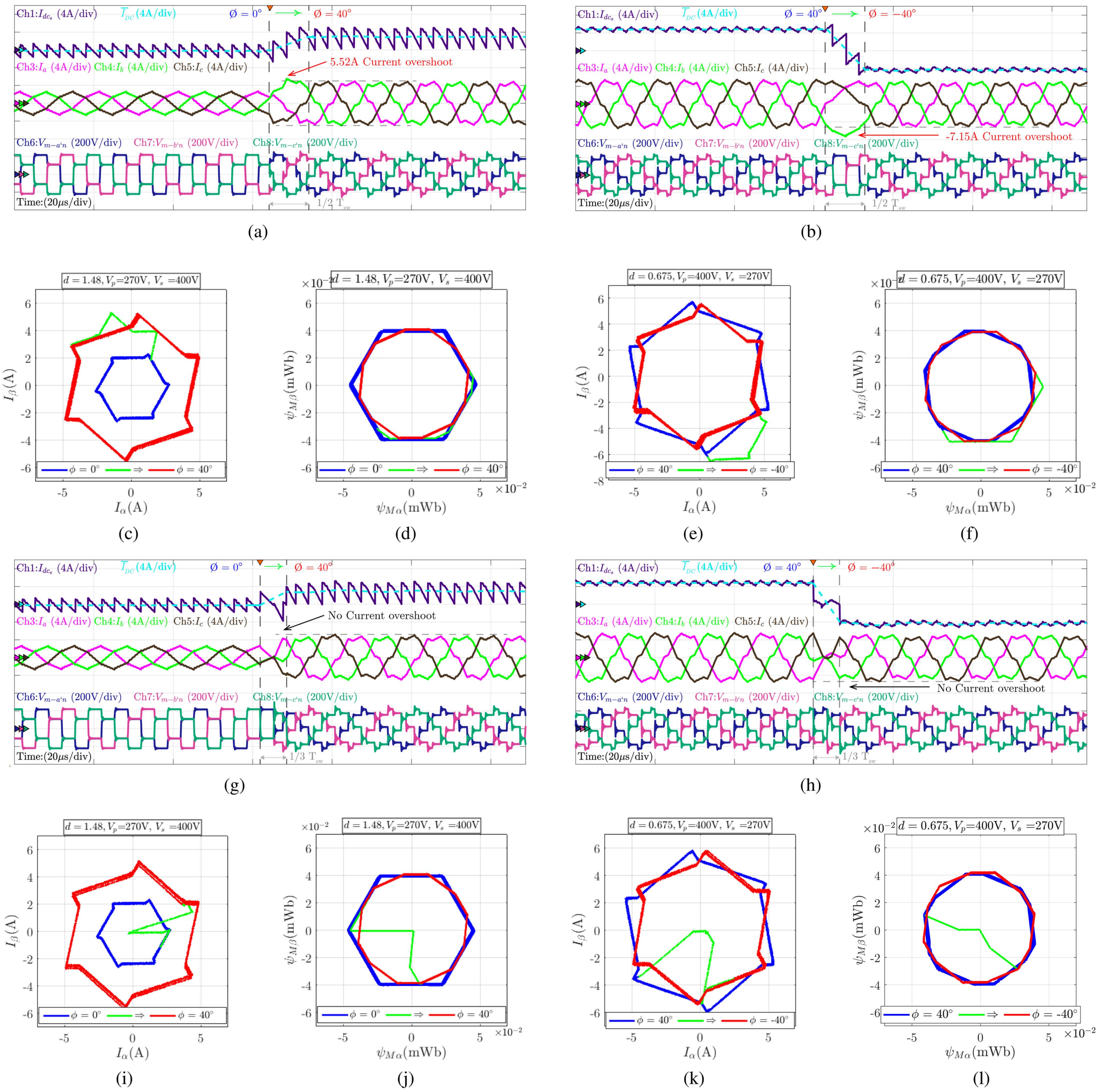

(a) (b) (c) (d) (e) (f) (g) (h) (i) (j) (k) (l)

Fig. 16. Experimental results for the conventional IFCC method and the proposed SS-IFCC method: Time domain (Ch1:I_{dc_s}/ $\bar{I}_{DC}$/ Ch3:I_a/ Ch4:I_b/ Ch5:I_c/ Ch6:$V_{m-a'n}$/ Ch7:$V_{m-b'n}$/ Ch8:$V_{m-c'n}$)—(a), (b), (g), (h) and trajectories of transformer currents—(c), (e), (i), (k), and magnetizing flux—(d), (f), (j), (l) in $\alpha\beta$ coordinates, for different gains and load-angle change. (a) Conventional IFCC, $d = 1.48$, 0° → 40°, time domain. (b) Conventional IFCC, $d = 0.675$, 40° → −40°, time domain. (c) Conventional IFCC, $d = 1.48$, 0° → 40°, current trajectory. (d) Conventional IFCC, $d = 1.48$, 0° → 40°, flux trajectory. (e) Conventional IFCC, $d = 0.675$, 40° →−40°, current trajectory. (f) Conventional IFCC, $d = 0.675$, 40° → −40°, flux trajectory. (g) Proposed SS-IFCC, $d = 1.48$, 0° → 40°, time domain. (h) Proposed SS-IFCC, $d = 0.675$, 40° → −40°, time domain. (i) Proposed SS-IFCC, $d = 1.48$, 0° → 40°, current trajectory. (j) Proposed SS-IFCC, $d = 1.48$, 0° → 40°, flux trajectory. (k) Proposed SS-IFCC, $d = 0.675$, 40° → −40°, current trajectory. (l) Proposed SS-IFCC, $d = 0.675$, 40° → −40°, flux trajectory.

instantaneous output port current I_{dc-s} and the average output dc current $\bar{I}_{DC}$ change from positive to negative values, reflecting the reversal in the power. A distinct current overshoot of −7.15 [see Fig. 16(b)] is observed, significantly exceeding the peak current operation of 5.37 A at rated power (an increase of over 30%), and thus, oversized inductors and devices with higher peak current rating are employed in hardware. While the transformer current and magnetizing flux-linkage trajectories reach the steady-state without any dc-bias, a high current overshoot can be observed in the transient trajectories. The transformer magnetizing flux is well bounded in the maximum envelope of $\phi = 0°$.

Similarly, the experimental results with the proposed SS-IFCC method for $d = 0.675$, $\phi = 40° \rightarrow -40°$ are shown in Fig. 16(h), (k), (l). As observed before, with the load-angle change with SS-IFCC method, the instantaneous output port current I_{dc-s} exhibits an irregular pattern, the capacitor at the output port filters the ripple, supplying the average output dc current $\bar{I}_{DC}$ to the output port, which inverts to demonstrate reversal in power. Consistent with previous results, no current overshoot or dc bias is observed in the transformer currents for this scenario as well, with the SS-IFCC method. The trajectories [see Fig. 16(i), (j)] exhibit a similar behavior, moving to the origin from the initial trajectory and then to the target trajectory without any dc bias or overshoot and enclosed in the maximum value envelope.

In all cases, the proposed SS-IFCC method ensures the transient current and flux trajectories reach the target trajectory without any dc bias and overshoot. The results validate the proposed SS-IFCC method and highlight its universal control across the entire voltage-gain operating range in contrast to the conventional IFCC, which exhibits current overshoots. Furthermore, the proposed method demonstrates robust control as it operates independently of the system parameters' knowledge, unlike the conventional IFCC, where the p-factor value is required to be determined based on the inductor ratios and operating port voltages. Also, the current overshoots with the conventional IFCC method obtained through the experimental results closely match the simulation results. The small differences arise due to nonidealities of the hardware setup, such as transformer winding resistance and dead time.

Furthermore, in the experiment results, it can be observed that the transient time with the conventional IFCC method is around $1/2$ of the switching period ($1/2 \times T_{\text{sw}}$) for both scenarios. In comparison, with the SS-IFCC method, the current and flux trajectory simultaneously reach the target steady state within two switching states or $1/3$ of the switching period($1/3 \times T_{\text{sw}}$), able to decrease the transient time by 33%.

After the load-angle change, a few minor oscillations can be observed in the hardware demonstration for both the conventional IFCC method and the proposed SS-IFCC method. It can also be inferred from the thicker target trajectories of the current (in red color) in the $\alpha\beta$ coordinates for both scenarios, especially in the case of power step-up, as shown in Fig. 16(c) and (i). These minor oscillations are due to the effect of non-negligible dead-time and winding resistance of the transformer, present in the hardware implementation. During the dead-time interval, current zero crossings lead to voltage-time errors being applied to the transformers' stray inductance. In the hardware implementation, a dead-time of 150 ns with 50-kHz switching frequency using SiC MOSFETs is implemented. It is important to note that for applications employing devices, such as IGBTs or IGCTs with lower switching frequencies, the dead-time could constitute a considerable portion of the switching period, thus requiring careful consideration to achieve genuine dead-beat behavior. However, a detailed exploration of solutions for this specific challenge falls outside the scope of this article.

The converter starts up and powers OFF with a load-angle of $\phi = 0°$. The start-up and power-OFF trajectories with the SS-IFCC method are shown in Figs. 17 and 18, respectively. Even at a load-angle of $\phi = 0°$, the current trajectory is not fixed to the origin as there is a current flowing because of the effects of dead-time, and is depicted in Fig. 17(a). The measured flux trajectory in power-OFF shown in Fig. 18(b) exhibits oscillations when moving to the origin due to the LC resonance between the switch capacitance and the inductor. Nonetheless, the trajectory reaches the steady state without any dc bias or overshoots, validating the seamless integration of the start-up and power-OFF strategies with the proposed SS-IFCC method.

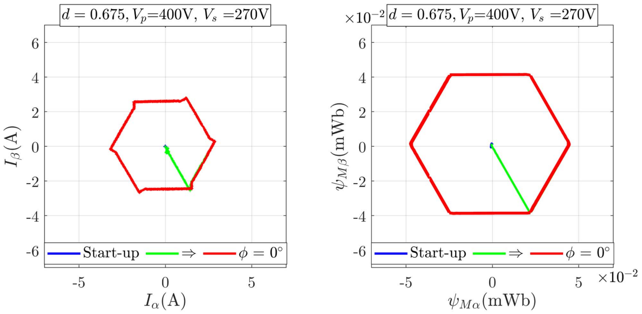

(a) (b)

Fig. 17. Trajectories of (a) transformer currents and (b) magnetizing flux for start-up with the proposed SS-IFCC.

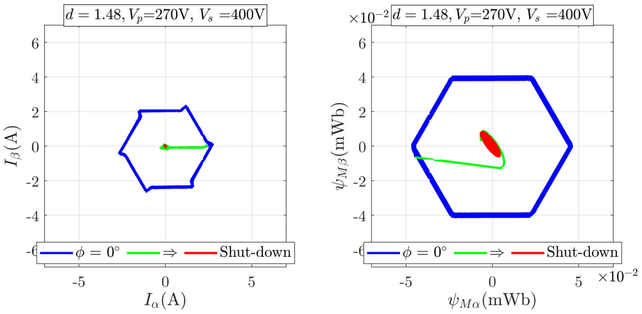

(a) (b)

Fig. 18. Trajectories of (a) transformer currents and (b) magnetizing flux for power-OFF with the proposed SS-IFCC.

VI. CONCLUSION

The article presented a highly dynamic control in SS-IFCC for DAB3 converter, which utilizes the switching sequences to eliminate the dc bias and overshoots in transformer currents and magnetizing flux dynamics for large and abrupt power changes. In contrast to the state-of-the-art methods, the SS-IFCC stands out due to it is straightforward implementation, universal applicability across all voltage gain scenarios, and inherent robustness as it functions independently of converter parameters. Comprehensive validation through both simulation and hardware experimental results, including a comparison with conventional IFCC, confirms the superior dynamic performance and robustness of the proposed SS-IFCC scheme for DAB3 converters. The methodology of the proposed SS-IFCC method for the DAB3 converter can potentially be extended to different winding configurations and multilevel bridge-based DAB3 converters.

REFERENCES

[1] R. W. A. A. De Doncker, D. M. Divan, and M. H. Kheraluwala, "A three-phase soft-switched high-power-density DC/DC converter for high-power applications," *IEEE Trans. Ind. Appl.*, vol. 27, no. 1, pp. 63–73, Jan./Feb. 1991.

[2] M. N. Kheraluwala, R. W. Gascoigne, D. M. Divan, and E. D. Baumann, “Performance characterization of a high-power dual active bridge DC-to-DC converter,” *IEEE Trans. Ind. Appl.*, vol. 28, no. 6, pp. 1294–1301, Nov./Dec. 1992.

[3] R. W. De Doncker, “Power electronic technologies for flexible DC distribution grids,” in *Proc. Int. Power Electron. Conf.*, 2014, pp. 736–743.

[4] F. D. Freijedo, E. Rodriguez-Diaz, and D. Dujic, “Stable and passive high-power dual active bridge converters interfacing MVDC grids,” *IEEE Trans. Ind. Electron.*, vol. 65, no. 12, pp. 9561–9570, Dec. 2018.

[5] A. Anurag, S. Acharya, S. Bhattacharya, T. R. Weatherford, and A. A. Parker, “A gen-3 10-kV SiC MOSFET-based medium-voltage three-phase dual active bridge converter enabling a mobile utility support equipment solid state transformer,” *IEEE Trans. Emerg. Sel. Topics Power Electron.*, vol. 10, no. 2, pp. 1519–1536, Apr. 2022.

[6] N. H. Baars, J. Everts, H. Huisman, J. L. Duarte, and E. A. Lomonova, “A 80-kW isolated DC–DC converter for railway applications,” *IEEE Trans. Power Electron.*, vol. 30, no. 12, pp. 6639–6647, Dec. 2015.

[7] J. Walter and R. W. De Doncker, “High-power galvanically isolated DC/DC converter topology for future automobiles,” in *Proc. IEEE 34th Annu. Conf. Power Electron. Specialist*, 2003, vol. 1, pp. 27–32.

[8] S. S. Shah and S. Bhattacharya, “A design optimization approach for dual active bridge converter for multiple vehicle classes with disparate input DC voltages,” in *Proc. IEEE Transp. Electrific. Conf. Expo*, 2020, pp. 566–573.

[9] C. Wang, P. Zheng, and J. Bauman, “A review of electric vehicle auxiliary power modules: Challenges, topologies, and future trends,” *IEEE Trans. Power Electron.*, vol. 38, no. 9, pp. 11233–11244, Sep. 2023.

[10] D. Wang, B. Nahid-Mobarakeh, and A. Emadi, “Second harmonic current reduction for a battery-driven grid interface with three-phase dual active bridge DC–DC converter,” *IEEE Trans. Ind. Electron.*, vol. 66, no. 11, pp. 9056–9064, Nov. 2019.

[11] M. Bragard, N. Soltau, S. Thomas, and R. W. De Doncker, “The balance of renewable sources and user demands in grids: Power electronics for modular battery energy storage systems,” *IEEE Trans. Power Electron.*, vol. 25, no. 12, pp. 3049–3056, Dec. 2010.

[12] N. M. L. Tan, T. Abe, and H. Akagi, “Design and performance of a bidirectional isolated DC–DC converter for a battery energy storage system,” *IEEE Trans. Power Electron.*, vol. 27, no. 3, pp. 1237–1248, Mar. 2012.

[13] H. A. B. Siddique and R. W. De Doncker, “Evaluation of DC collector-grid configurations for large photovoltaic parks,” *IEEE Trans. Power Del.*, vol. 33, no. 1, pp. 311–320, Feb. 2018.

[14] T. Jimichi, M. Kaymak, and R. W. De Doncker, “Design and experimental verification of a three-phase dual-active bridge converter for offshore wind turbines,” in *Proc. Int. Power Electron. Conf.*, 2018, pp. 3729–3733.

[15] S. P. Engel, N. Soltau, H. Stagge, and R. W. De Doncker, “Dynamic and balanced control of three-phase high-power dual-active bridge DC–DC converters in DC-grid applications,” *IEEE Trans. Power Electron.*, vol. 28, no. 4, pp. 1880–1889, Apr. 2013.

[16] S. P. Engel, N. Soltau, H. Stagge, and R. W. De Doncker, “Improved instantaneous current control for high-power three-phase dual-active bridge DC–DC converters,” *IEEE Trans. Power Electron.*, vol. 29, no. 8, pp. 4067–4077, Aug. 2014.

[17] J. Hu, S. Cui, S. Wang, and R. W. De Doncker, “Instantaneous flux and current control for a three-phase dual-active bridge DC–DC converter,” *IEEE Trans. Power Electron.*, vol. 35, no. 2, pp. 2184–2195, Feb. 2020.

[18] R. Goldbeck, J. Hu, and R. W. De Doncker, “Improved instantaneous flux and current control for three-phase dual-active bridge DC-DC converters,” in *Proc. IEEE Energy Convers. Congr. Expo.*, 2021, pp. 2784–2791.

[19] J. Huang, Z. Li, L. Shi, Y. Wang, and J. Zhu, “Optimized modulation and dynamic control of a three-phase dual active bridge converter with variable duty cycles,” *IEEE Trans. Power Electron.*, vol. 34, no. 3, pp. 2856–2873, Mar. 2019.

[20] Z. Li, Y. Wang, Y. Cui, L. Shi, J. Huang, and W. Lei, “Fast transient current control for three-phase dual-active-bridge DC-DC converters with variable duty cycles,” in *Proc. IEEE Appl. Power Electron. Conf. Expo.*, 2017, pp. 1209–1215.

[21] H. Chen, J. Liu, S. Du, C. Li, and Z. Deng, “A novel fast transient current scheme for three phase dual active bridge with asymmetrical phase-shift control,” in *Proc. 11th Int. Conf. Power Electron.*, 2023, pp. 2820–2824.

[22] J. Yun, S. Cui, and S.-K. Sul, “Instantaneous dual flux control for three-phase dual-active bridge,” in *Proc. IEEE Energy Convers. Congr. Expo.*, 2023, pp. 2747–2751.

[23] J. Yun, S. Cui, and S.-K. Sul, “Generalized instantaneous dual flux control for three-phase dual-active bridge converter,” in *Proc. IEEE Appl. Power Electron. Conf. Expo.*, 2024, pp. 440–444.

[24] J. Yun, S. Cui, and S.-K. Sul, “Instantaneous pulse pattern control for optimized dynamic performance of three-phase dual-active bridge converter,” *IEEE Trans. Power Electron.*, vol. 40, no. 7, pp. 9019–9033, Jul. 2025.

[25] N. Wang, Y. Wang, W. Hu, J. Chen, Z. Li, and Z. Chen, “A PSO-ANN-aided DC-bias current suppression strategy for three-phase DAB converter with variable duty cycles,” *IEEE Trans. Ind. Electron.*, vol. 72, no. 2, pp. 1586–1596, Feb. 2025.

[26] A. Agarwal and S. Bhattacharya, “Design considerations for a three-phase dab with instantaneous flux and current control under wide voltage variation,” in *Proc. IEEE Energy Convers. Congr. Expo.*, 2024, pp. 2993–3000.

[27] D. von den Hoff and R. W. De Doncker, “Instantaneous start-up and shutdown method for three-phase dual-active bridge DC-DC converters,” in *Proc. IEEE Energy Convers. Congr. Expo.*, 2019, pp. 5210–5216.

Apoorv Agarwal (Member, IEEE) received the B.Tech. degree in electrical engineering from Pandit Deendayal Petroleum University, Gujarat, India, in 2017, and the M.S. degree in electrical engineering from North Carolina State University, Raleigh, NC, USA, in 2019. He is currently working toward the Ph.D. degree in electrical and computer engineering with FREEDM Systems Center, North Carolina State University, Raleigh, NC, USA.

His research interests include modeling and control of dc–dc converters for energy storage systems and the integration of renewable energy.

Subhashish Bhattacharya (Fellow, IEEE) received the B.E. degree from University of Roorkee (IIT-Roorkee), Roorkee, India, in 1986, the M.E. degree from Indian Institute of Science, Bengaluru, in 1988, India, and the Ph.D. degree from University of Wisconsin-Madison, Madison, WI, USA, in 2003, all in electrical engineering.

He was with FACTS and Power Quality Division at Westinghouse R&D and Siemens Power Transmission and Distribution, from 1998 to 2005. He is currently the Duke Energy Distinguished Professor with the Department of ECE, NC State University. He joined NCSU in August 2005, where he is a founding faculty member of NSF FREEDM Center, ATEC, and DoE PowerAmerica Institute. A part of his Ph.D. research on active power filters was commercialized by York Corporation [now Johnson Controls]. His research interests include solid-state transformers with HV SiC devices, integration of renewable energy resources, microgrids, high-frequency magnetics, active filters, and the application of new power semiconductor devices such as SiC and GaN for power converters. His research is funded by several industries, NSF, DoE/ARPA-E, Navy, NASA, and others. He has over 900 publications, 12 patents, H-index of 80, and 27,100+ citations.